Reduced Cu/Pt–$HCa_2Ta_3O_{10}$ Perovskite Nanosheets for Sunlight-Driven Conversion of CO_2 into Valuable Fuels

*Nhu-Nang Vu, Chinh-Chien Nguyen, Serge Kaliaguine, and Trong-On Do**

Reduced perovskite $HCa_2Ta_3O_{10}$ nanosheets loaded with Pt and Cu are synthesized for sunlight-driven conversion of CO_2 with water vapor into valuable fuels. Perovskite nanosheets are prepared by exfoliating layered perovskite $CsCa_2Ta_3O_{10}$ via tetra butyl ammonium ion exchange, followed by liquid ultrasonic exfoliation. The obtained nanosheets exhibits a high specific surface area (>200 $m^2\ g^{-1}$). The photocatalytic performance of the resulting reduced perovskite nanosheets is evaluated for CO_2 photoreduction under sunlight in the presence of saturated water vapor. The reduced nanosheets exhibit much higher photoactivity than the nonreduced ones. This can be ascribed to their unique structure. The hydrogen treatment in the presence of platinum induces a considerable amount of Ta^{+4} and oxygen vacancies, which apparently improves the visible light absorption of perovskite nanosheets. Moreover, the introduction of CuO nanoparticles significantly improves the electron–hole separation through the formation of a p–n junction. It also enhances the adsorption of CO_2 and stabilizes C1 intermediates which are favorable for C—C coupling to form C2 products (e.g., ethanol). The formation rates of ethanol and methanol are 113 and 7.4 μmol $g^{-1}\ h^{-1}$, respectively, while only methanol is obtained at the rate of 125.9 μmol $g^{-1}\ h^{-1}$ in the absence of CuO nanoparticles.

1. Introduction

Currently, our energy supply mainly originates from fossil resources such as coal, oil, and natural gas, occupying 80% of the total world energy supply.[1] However, the combustion of fossil fuels releases a significant amount of CO_2 as a primary greenhouse gas into the atmosphere, leading to an increase in atmospheric CO_2 concentration. The enormous consequences of global warming associated with this increase have driven research interests in developing breakthrough technologies that facilitate the recycling of CO_2. Among existing approaches, photocatalytic reduction of CO_2 to renewable fuels, using sunlight is an avenue for sustainable development, as it can address both the global warming and energy shortage problems.[2] Since Inoue et al. published the first report of photoreduction of CO_2 into organic compounds in 1979,[3] a variety of photocatalysts has been developed for CO_2 photoreduction.[2a,4] Among these materials, perovskite-based photocatalysts offer many feasible characteristics for CO_2 photoreduction due to their high stability, crystallinity, as well as excellent charge separation properties.[5] Notably, layered perovskite materials are considered to be active photocatalysts because they are associated with a structure favorable for charge separation and transfer, deposition of cocatalysts, and selective intercalation of reactants.[6]

Recently, Dion–Jacobson type layered perovskites of $AB_2Ta_3O_{10}$ (A = Cs, K, Na; B = Ca, Ba, Sr) were widely studied for photocatalytic processes such as water splitting and pollutant degradation, due to their interesting properties including ion exchange, exfoliation, electrical and electrochemical properties, electronic/protonic conductivity, and high crystallinity.[7] However, low specific surface area limits their efficiency in photocatalysis. Featuring 2D perovskite nanosheets exfoliated from these materials has been regarded as a compelling solution. 2D nanosheets with small particle size lead to a larger surface area, which bears more active sites exposed on the surface for photocatalytic reaction. Moreover, these 2D nanosheets benefit from a shorter transfer pathway for charge carriers to quickly reach their surface without being recombined or trapped at defect sites, thus leading to higher efficiency compared to non-exfoliated perovskites.[8] Nonetheless, little information has been reported for the fabrication of 2D perovskite nanosheets for CO_2 photoconversion. Their wide band gap (>3 eV) enables them to work however only in the UV range ($\lambda < 400$ nm) which constitutes only about 5% energy of the incident sunlight.[9] Considering the large fraction of visible light (about 43%) in sunlight, it is highly desirable to develop a photocatalyst with an efficient response under visible irradiation. In the last decades, researchers have explored many different strategies to address the drawbacks of the limited sunlight absorption such as band structure engineering and heterostructure design.[10] The most recent approach is to engineer the band structure of TiO_2 via hydrogen treatment that shows a significant influence on both visible light absorption and photocatalytic activity.[11] Heating TiO_2 under hydrogen resulted in the formation of Ti^{+3} and oxygen vacancies in the TiO_x matrix which narrows the band gap and turns white TiO_2 into black TiO_2.[12] To the best of our knowledge, no study on hydrogen treatment of perovskite compounds has been reported, which motivated us to apply

N.-N. Vu, C.-C. Nguyen, Prof. S. Kaliaguine, Prof. T.-O. Do
Department of Chemical Engineering
Laval University
Québec G1V 0A6, Canada
E-mail: trong-on.do@gch.ulaval.ca

DOI: 10.1002/adsu.201700048

this strategy to develop an efficient sunlight-driven perovskite-based photocatalyst for CO_2 photoreduction.

In the present work, we report the first synthesis of reduced Cu/Pt–$HCa_2Ta_3O_{10}$ perovskite nanosheets via exfoliation followed by hydrogen treatment. The formation of oxygen vacancies in Pt-containing perovskite nanosheets by hydrogen treatment led to a decrease in band gap and simultaneously generated active sites for CO_2 adsorption and activation. The reduced Pt nanosheets exhibit much higher photocatalytic activity than the nonreduced ones under sunlight. Furthermore, only methanol was obtained for the reduced Pt nanosheets, while ethanol was formed as the primary product in the presence of CuO nanoparticles in the reduced Pt–perovskite nanosheets.

2. Result and Discussion

2.1. Synthesis and Characterization

Table 1 summarizes the physicochemical properties of a series of samples obtained at different steps of the treatment. The exfoliation steps resulted in an improvement of both the particle size and specific surface area. The obtained nanosheets exhibited very high specific area, even after the removal of the tetra butyl ammonium (TBA) by calcination. The hydrogen treatment did not affect the size and the specific surface area.

Powder X-ray diffraction (XRD) patterns of the bulk $CsCa_2Ta_3O_{10}$, Cal-CNP, and R-Pt/Cu-CNP samples are shown in **Figure 1**. The XRD pattern of bulk $CsCa_2Ta_3O_{10}$ matches well with that of $CsCa_2Ta_3O_{10}$ perovskite powder reported previously.[13] The single phase associated to tetragonal symmetry with P4/*mmm* space group (a = 0.38672 nm; c = 1.55323 nm) was found.[14] The XRD pattern of Cal-CNP displays broader and weaker peaks as compared to the originally layered perovskite, suggesting a less ordered lamellar structure as well as reduction of the crystallite size. In Cal-CNP, only diffraction peaks of (00*l*) and (*hk*0) planes were observed, whereas no diffraction peaks for (*hkl*) planes were detected, suggesting that the layered perovskite structure was disordered upon exfoliation and calcination. Moreover, diffraction peaks of (100) and (110) planes indicate the preservation of the 2D structure of perovskite sheets

Table 1. Physicochemical properties of the various samples. TBA-CNP: TBA–$Ca_2Ta_3O_{10}$ nanosheets; Cal-CNP: Calcined $HCa_2Ta_3O_{10}$ nanosheets; R-Pt/Cu-bulk: Reduced Pt/Cu bulk $CsCa_2Ta_3O_{10}$; R-Pt-CNP: Reduced Pt–$HCa_2Ta_3O_{10}$ nanosheets; R-Pt/Cu-CNP: Reduced Pt/Cu–$HCa_2Ta_3O_{10}$ nanosheets.

Sample	Specific area [m^2 g^{-1}]	Crystallite size[a] [nm]	Crystallite size[b] [nm]
Bulk-$CsCa_2Ta_3O_{10}$	11	>1000	>1000
TBA-CNP	314	–	–
Cal-CNP	210	18–21	19–23
R-Pt/Cu-bulk	5	–	–
R-Pt-CNP	207	18–21	–
R-Pt/Cu-CNP	205	18–21	19–23

[a]Calculated using Scherrer equation; [b]Calculated using TEM.

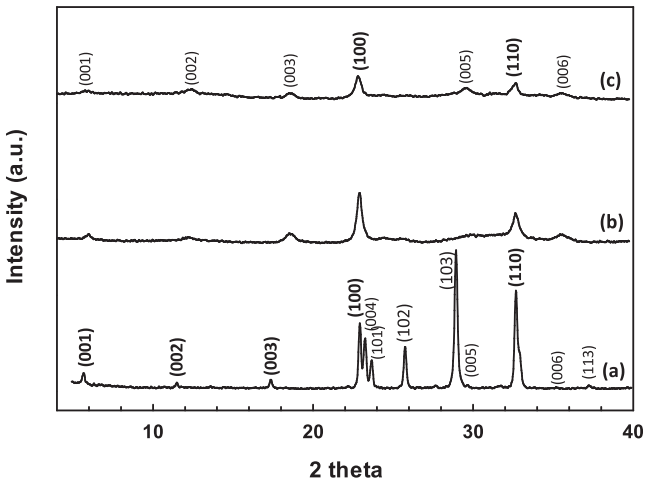

Figure 1. XRD pattern of (a) bulk $CsCa_2Ta_3O_{10}$, (b) Cal-CNP, (c) R-Pt/Cu-CNP.

even after exfoliation and calcination.[15] The crystallite size of nanosheets calculated using Scherrer equation is 18 and 23 nm for (100) and (110) peaks, respectively. These values indicate the significant decrease in crystallite size from micro- to nanosize upon exfoliation.[6b] For the R-Pt/Cu-CNP sample (e.g., in the presence of Pt and Cu) after hydrogen treatment, no significant change of peak intensity in the XRD pattern as compared to the sample before hydrogen treatment indicates that the perovskite structure and nanoparticles size were retained after this treatment (Figure 1c). Also, the peaks characteristic of Pt and Cu are essentially not visible, owing to low Cu and Pt loading and very small particle size.

Figure 2A shows the water suspension of TBA-CNP obtained after the exfoliation and centrifugation. The suspension is clear, suggesting the nanosize of TBA-CNP sample. TBA^+ ions play a crucial role in the synthesis of TBA-CNP. The acid–base reaction between the protonated form ($H\text{-}Ca_2Ta_3O_{10}$) and TBA-OH leads to the intercalation of bulky TBA^+ ions into interlayers, resulting in the exfoliation. The nanosheet suspension has a concentration of about 0.4 g L^{-1}. Figure 2B provides a clear Transmission Electron Microscopy (TEM) image of nanosheets after calcination (Cal-CNP) with a distinct edge and uniform size. Interestingly, the sample is composed of discrete particles rather than aggregates. Nanosheets were protected against dramatic aggregation during the calcination, owing to TBA ions being grafted on the CNP surface. The average size of nanosheets is about 18–21 nm as determined from this picture. As seen in Figure 2C, for a high-resolution TEM (HR-TEM) image, lattice spacings commensurate with 0.386 and 0.281 nm are found, corresponding to the (100) and (110) planes of nanosheets. The presence of (100) and (110) planes in the perovskite nanosheet structure are more clearly observed in the fast Fourier transformed (FFT) pattern shown in Figure 2D.

The amount of TBA^+ ions grafted on the CNP surface was determined by thermogravimetric analysis (TGA) as shown in **Figure 3**. The weight loss below 100 °C is 3.2%, which can be ascribed to the evaporation of surface absorbed water. The large weight loss of 9.8% between 100 and 550 °C, which can be attributed to the decomposition of TBA molecules,

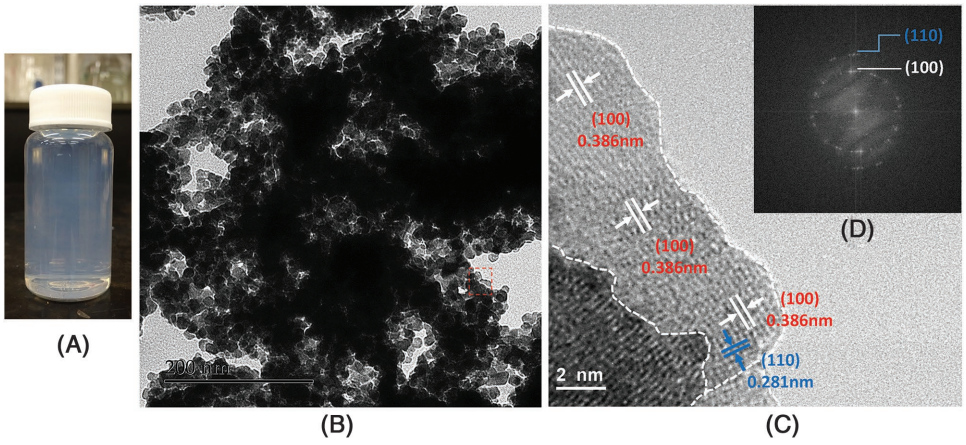

Figure 2. A) The physical appearance of nanosheet suspension of TBA-CNP, B) TEM images of Cal-CNP, C,D) HRTEM and (fast Fourier transformed) FFT pattern of perovskite nanosheets.

corresponds to the content of TBA ions intercalated between the surface of nanosheets. The molar percentage of TBA in TBA-CNP nanosheets calculated from this weight loss is ≈30.04%. This value is also the percentage of the number of initial Cs ions which were exchanged with TBA ions during the exfoliation.

According to the Brunauer-Emmett-Teller (BET) analysis (Figure S3 (Supporting Information) and Table 1), the specific surface area of TBA-CNP is 314 $m^2 g^{-1}$, which is much higher than that of the bulk material (11 $m^2 g^{-1}$). This is due to the size of particles in the sample of nanosheets compared to that of the bulk material. After calcination, the specific surface area of TBA-CNP sample is decreased to 210 $m^2 g^{-1}$. This result indicates no serious aggregation of perovskite nanoparticles after calcination. The surface of nanosheets was intercalated by TBA^+ ions, which prevents them from aggregating. Furthermore, for the reduced Pt/Cu-CNP samples, denoted as R-Pt/Cu-CNP, no significant change in surface area was found as compared to that of the Cal-CNP sample, indicating no effect of the H_2 reduction on the specific surface area and particle nanosize (Table 1).

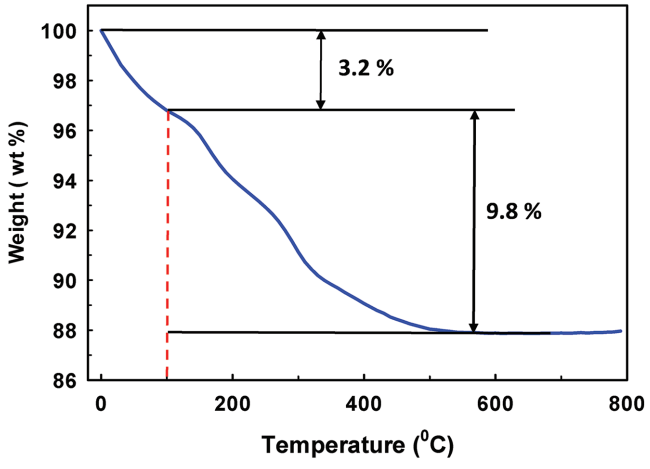

Figure 3. TGA curve for TBA-CNP sample.

Figure 4A shows a TEM image along with the corresponding Selected Area Electron Diffraction (SAED) pattern of the Pt/Cu-CNP sample after H_2 treatment (namely R-Pt/Cu-CNP). It can be observed that nanoparticles of both Cu and Pt are highly dispersed on the surface of perovskite nanosheets. The SAED pattern (Figure 4A inset) exhibits mixed diffraction rings that can be indexed to (100) and (110) planes of perovskite nanosheets. Figure 4B shows a high-resolution TEM of the same samples, indicating that no structural disorder was induced by H_2 treatment. The size of nanoparticles is in the range of 4–7 nm. This is consistent with the XRD results, showing no metallic phase and no other crystalline lattice except CNP (Figure 1(c)). For further determination of nanoparticle composition, Energy Dispersive Spectroscopy (EDS) studies were thoroughly carried out on different nanoparticles (Figure 4C,D). The results indicate that Pt-rich and Cu-rich particles are distributed on the surface of perovskite nanosheets. Figure 4E shows a high-resolution TEM image of a Cu-rich particle, a lattice spacing of 0.252 nm is observed, which corresponds to (002) plane of CuO. Nanoparticles made up of both Cu and Pt are also found in this R-Pt/Cu-CNP sample (**Figure 5**).

Figure 6 shows UV–vis spectra of the Cal-CNP, Cal-Pt/Cu-CNP, and R-Pt/Cu-CNP samples. Both samples Cal-CNP and Cal-Pt/Cu-CNP (after calcination) absorb only UV light (λ < 400 nm), while R-Pt/Cu-CNP shows an enhanced visible light absorption, which is compatible with the color change from white to gray after H_2 treatment. As a result, R-Pt/Cu-CNP sample absorbs sunlight more efficiently (e.g., absorption of both UV and visible light) upon H_2 treatment. The simultaneous presence of Pt and Cu slightly increases the visible light absorption of Cal-Pt/Cu-CNP as shown in Figure 6(b). This enhancement is however not high compared to R-Pt/Cu-CNP. This result indicates the significant impact of the H_2 reduction on visible light absorption. The presence of platinum plays a key role for the chemisorption and subsequent dissociation of H_2 molecules to form very active hydrogen atoms (hydrogen spillover) which then participate in H_2 reduction.[16]

Figure S4 (Supporting Information) displays X-ray photoelectron spectroscopy (XPS) survey and Ca 2p high-resolution XPS spectra of R-Pt/Cu-CNP, Cal-CNP, and in situ R-Pt/Cu-CNP

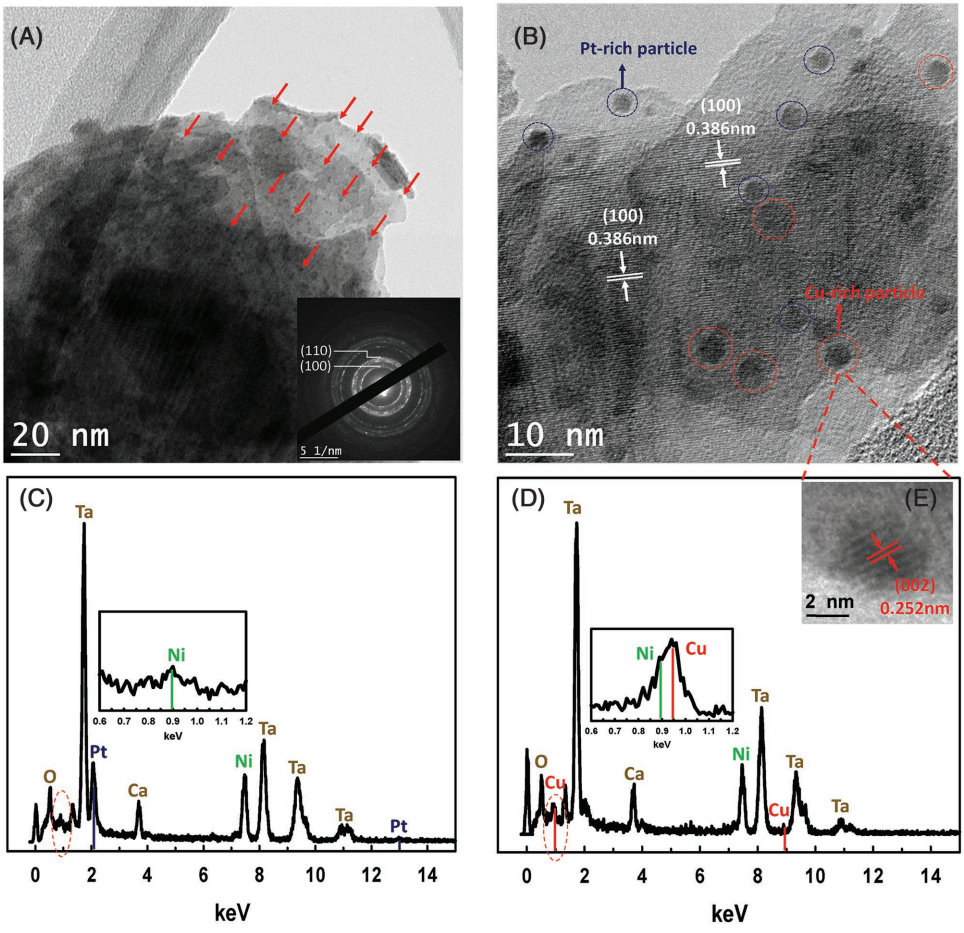

Figure 4. A) TEM with corresponding Selected Area Electron Diffraction (SAED) pattern of R-Pt/Cu-CNP (red arrows indicate the possible location of either Pt-rich particles and Cu-rich particles). B) HR-TEM image of R-Pt/Cu-CNP; EDS of (C) Cu-rich nanoparticles and (D) Pt-rich nanoparticles. E) HR-TEM image of a Cu-rich particle (Ni from TEM grid).

samples. The peak location of Ca 2p is essentially identical for the three samples. Ca 2p XPS spectrum shows two peaks at the binding energy of 348 and 352 eV which are assigned for Ca^{2+}. The XPS lines of Ta and O in nanosheet samples are shown in **Figure 7**. XPS spectra of Ta 4f are shown in Figure 7A. For Cal-CNP sample, there are two XPS peaks at 26.3 and 28.2 eV which are characteristic of Ta^{+5} in tantalum oxide.[17] However, after H_2 treatment, R-Pt/Cu-CNP sample exhibits different

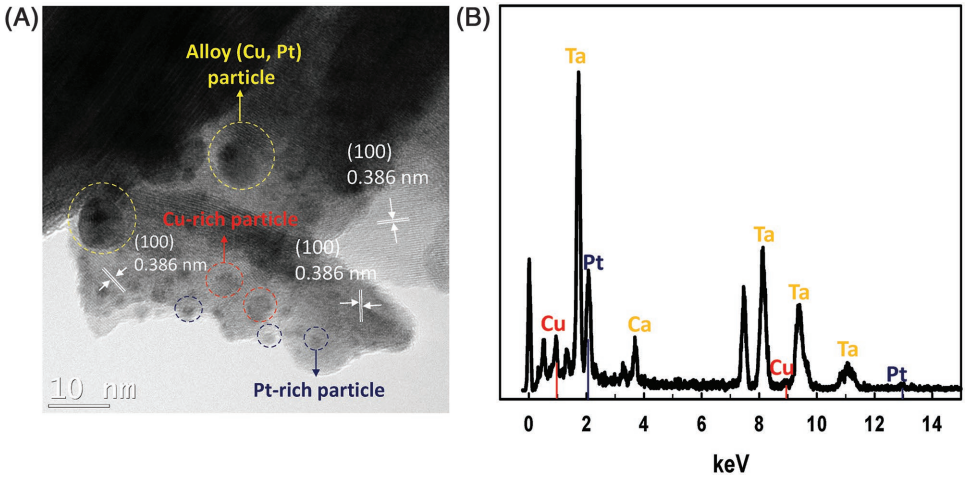

Figure 5. A) HR-TEM image of R-Pt/Cu-CNP and (B) EDS analysis of an alloy Pt–Cu nanoparticle.

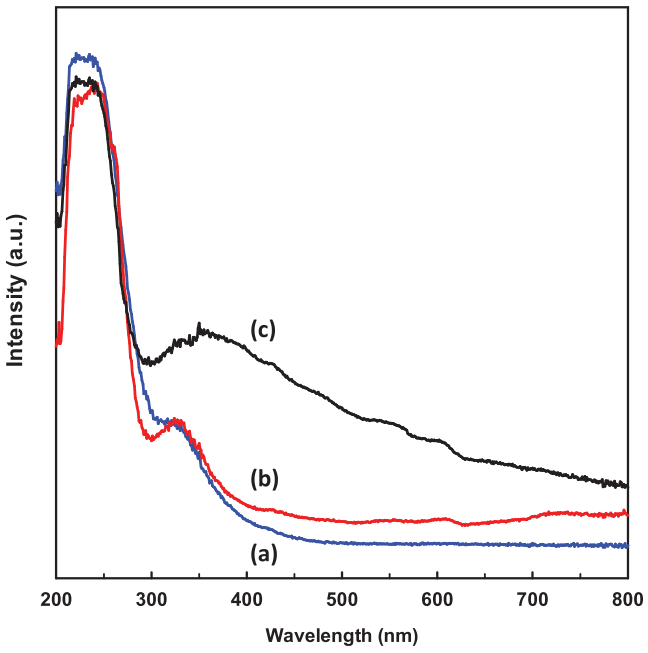

Figure 6. UV–vis spectra of (a) Cal-CNP, (b) Cal-Pt/Cu-CNP (*), and (c) R-Pt/Cu-CNP (*). (*): Sample obtained by calcining $HCa_2Ta_3O_{10}$ nanosheet loaded Pt/Cu in air.

oxidation state for Ta. As seen in XPS spectrum of R-Pt/Cu-CNP sample (Figure 7A), two XPS peaks with very low intensity at 24.7 and 26.6 eV assigned for Ta^{+4} are unambiguously observed, as expected for the formation of a small amount of Ta^{+4} through the reduction of Ta^{+5} under H_2 atmosphere.[18] The formation of Ta^{4+} is more clearly observed in the XPS spectrum of in situ R-Pt/Cu-CNP, showing a clear shift of 1.6 eV to lower binding energy corresponding to the XPS peaks of Ta^{+4}. The difference in concentration of Ta^{+4} between R-Pt/Cu-CNP and in situ R-Pt/Cu-CNP samples is mainly due to the high instability of Ta^{+4} which is easily reoxidized to Ta^{+5} by oxygen in the air.[19] Ta^{+4} found in the samples of nanosheets after H_2 treatment suggests the presence of oxygen vacancies in the perovskite structure of the reduced sample. It is worth to note that, the presence of oxygen vacancies yields mid-gap states in the forbidden area of CNP band structure below the conduction band, resulting in a decrease of the band gap and excitation energy.[12,20] Therefore, sunlight absorption is significantly improved. Additionally, oxygen vacancies can act as trapping site for photogenerated electrons, which prevents them from recombination and leads to higher photocatalytic activity.[21]

Figure 7B displays the O 1s XPS spectra of these three samples: Cal-CNP, R-Pt/Cu-CNP, and in situ R-Pt/Cu-CNP. O 1s XPS spectra can be fitted with three components at the binding energy of 530.2, 531.5, and 532.7 eV, which are characteristics of lattice oxygen in TaO_3^-, surface OH group (Ta—OH) and adsorption water (H_2O), respectively.[22] However, an increase in the concentration of surface OH groups is observed in reduced nanosheets samples where the in situ R-Pt/Cu-CNP has the highest amount of surface OH groups. This result is compatible with the increase of Ta^{+4} species, suggesting a close relationship between the concentration of surface OH groups and the formation of Ta^{+4} species or oxygen vacancies. During the H_2 treatment, in the presence of Pt, H_2 molecules dissociate to active H-atoms and bond to lattice oxygen atoms to form OH groups. This bond elongates and weakens the Ta—O bond, thus leading to the formation of Ta^{+4} or oxygen vacancies by the dissociation of water molecules under the thermal annealing.[23]

High-resolution XPS spectra of Cu and Pt elements in R-Pt/Cu-CNP are shown in Figure S5 (Supporting Information). The Cu 2p3/2 XPS spectrum shows one main peak at the binding energy of 934 eV and three shake-up satellites at the higher binding energy, which are characteristic of Cu^{2+}.[24] This result, in combination with HRTEM results, indicates the major oxidation of the Cu nanoparticle surface in the form of CuO. Cu-rich nanoparticles were possibly formed with an outer Pt core–shell

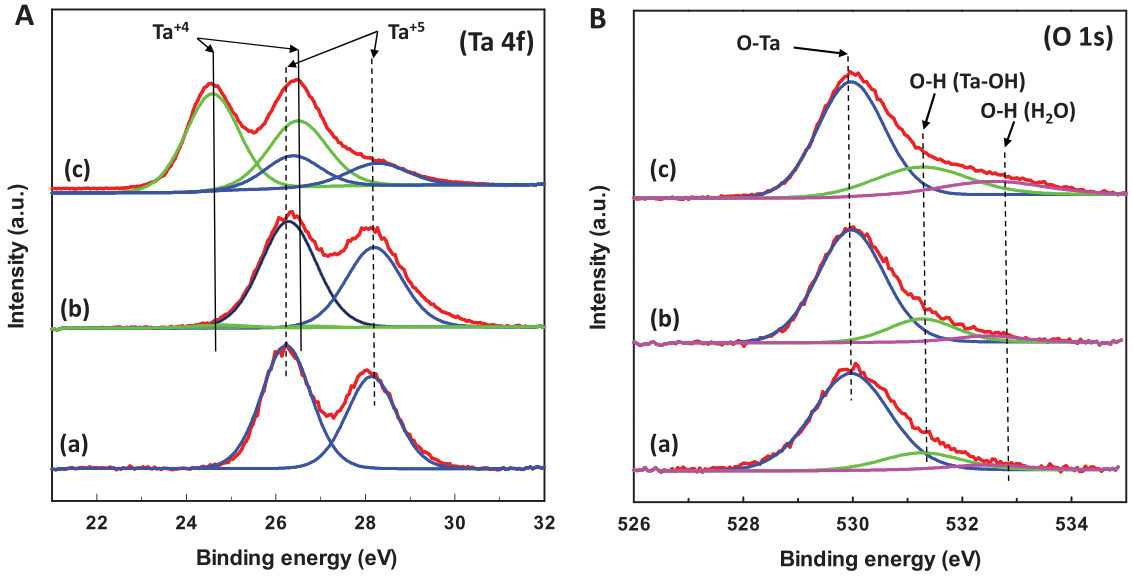

Figure 7. High-resolution XPS of A) Ta 4f and B) O 1s; (a) Cal-CNP, (b) R-Pt/Cu-CNP, and (c) in situ R-Pt/Cu-CNP (**). (**): Sample prepared by H_2 reduction of $HCa_2Ta_3O_{10}$ nanosheet loaded Pt/Cu in the reaction chamber of the XPS spectrometer.

Table 2. Photocatalytic activity of sunlight-driven CO_2 conversion for various reduced photocatalysts. R-Pt/Cu-CNP: Reduced Pt/Cu–$HCa_2Ta_3O_{10}$ nanosheets, R-Pt-CNP: Reduced Pt–$HCa_2Ta_3O_{10}$ nanosheets, R-Pt/Cu-bulk: Reduced Pt/Cu–$CsCa_2Ta_3O_{10}$.

Sample	Loaded cocatalyst [%]		Highest rate of the products [μmol g^{-1} h^{-1}]		Selectivity [%]	
	Pt	Cu	Methanol	Ethanol	Methanol	Ethanol
R-Pt/Cu-bulk	1.98	0.97	<0.1	ND	ND	ND
R-Pt-CNP	2.02	0	125.9	ND	100	ND
R-Pt/Cu-CNP	2.05	0.96	7.4	113.2	5.3	94.7

during the synthesis which prevents copper oxide from being H_2 reduced. The formation of oxide might have also resulted from exposure to air during the storage and transportation between measurements.[25] To date, this occurrence has not been reported, thus needing an accurate determination in further studies. The Pt 4f XPS spectrum could be fitted with three peaks: two peaks at the binding energy of 71.4 and 74.7 eV are characteristic of Pt metal, while the broad peak at a higher binding energy of 76.6 eV is characteristic of Cu 3p.[26]

Figure S6 (Supporting Information) displays SEM–EDX mapping of Ca, Ta, Cu, Pt, and O in the R-Pt/Cu-CNP sample. It can be seen that the elements such as Cu and Pt are uniformly distributed in the sample.

2.2. Photocatalytic Activity

Photocatalytic tests were carried out under ambient conditions as a function of reaction time (up to 10 h), using 20 mg of photocatalyst under simulated sunlight (100 mW cm^{-2}). A bulk sample ($CsCa_2Ta_3O_{10}$) loaded with the same contents of Pt and Cu (about 2% Pt and 1% Cu) was also treated with hydrogen under the same condition (denoted as R-Pt/Cu-bulk) and used for comparison with the reduced nanosheet sample (R-Pt/Cu-CNP). **Table 2** summarizes the results of CO_2 photoreduction over these reduced samples. The bulk $CsCa_2Ta_3O_{10}$, TBA-CNP, and Cal-CNP samples with the same Pt and Cu loading, however, without hydrogen treatment did not show any photocatalytic activity under the same photocatalytic reaction conditions (Table S1, Supporting Information).

Figure 8 shows the evolution in relative concentration of CO_2 as a function of photoreaction time over various photocatalysts. The reduced bulk sample loaded with Pt and Cu (R-Pt/Cu-bulk) had a very low photocatalytic activity for CO_2 conversion. Interestingly, for the sample of reduced nanosheets (R-Pt/Cu-CNP), the photoactivity is much higher with about 14% of CO_2 converted after 10 h. The reason for this high efficiency could be due to the advantages of nanosheets which included a high specific surface area and a short electron–hole travel pathway. The R-Pt/CNP sample bearing no CuO nanoparticles exhibited only 4% of CO_2 conversion after the same reaction time (10 h). From these results, it can be concluded that CuO nanoparticles play an important role as cocatalyst for the photoconversion of CO_2.

The evolution of CO_2 photoconversion products is plotted as a function of time over the reduced nanosheet samples in absence and presence of CuO: R-Pt/CNP, R-Pt/Cu-CNP in **Figure 9**A,B, respectively. Methanol as the primary product was observed for R-Pt/CNP. In contrast, ethanol and methanol were generated over R-Pt/Cu-CNP where ethanol was the primary product. The selectivity of methanol and ethanol after the 10 h reaction were 5.3% and 94.7%, respectively. Thus, the cocatalyst nature plays a key role in the production of the final products. In this study, Pt nanoparticles contribute to the formation of methanol, while coupling CuO and Pt nanoparticles lead to the formation of both methanol and ethanol.

The formation rate of each product was calculated based on the product evolution, time of reaction, and amount of photocatalyst. Figure 9C,D, respectively, shows the formation rate of each product of CO_2 conversion as the function of reaction time. It can be seen that the production rate of each product declines after few hours of the reaction. It can presumably be due to the accumulation of the intermediates and/or products adsorbed on the surface of the photocatalyst. This accumulation persists in the subsequent steps of the CO_2 reduction mechanism, thus resulting in a decrease of the evolution rate of products. The highest formation rate of methanol for R-Pt/CNP is 125.9 μmol g^{-1} h^{-1} after 2 h of the reaction. Reduced nanosheets loaded with both Pt and Cu (R-Pt/Cu-CNP) generated ethanol and methanol at the highest rate of 113.2 and 7.4 μmol g^{-1} h^{-1}, respectively. Particularly, the formation of methanol reaches the

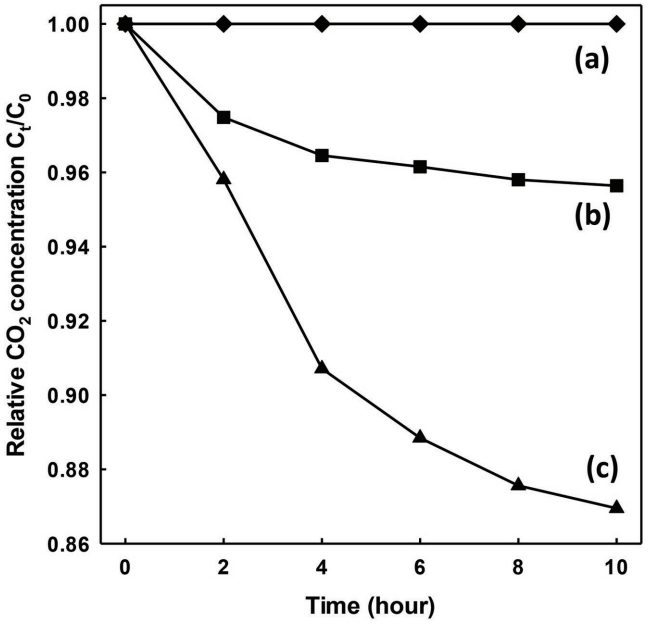

Figure 8. Relative CO_2 concentration (C_t/C_0) evolution as function of photoreaction time, (a) R-Pt/Cu-bulk $Ca_2Ta_3O_{10}$, (b) R-Pt-CNP, (c) R-Pt/Cu-CNP.

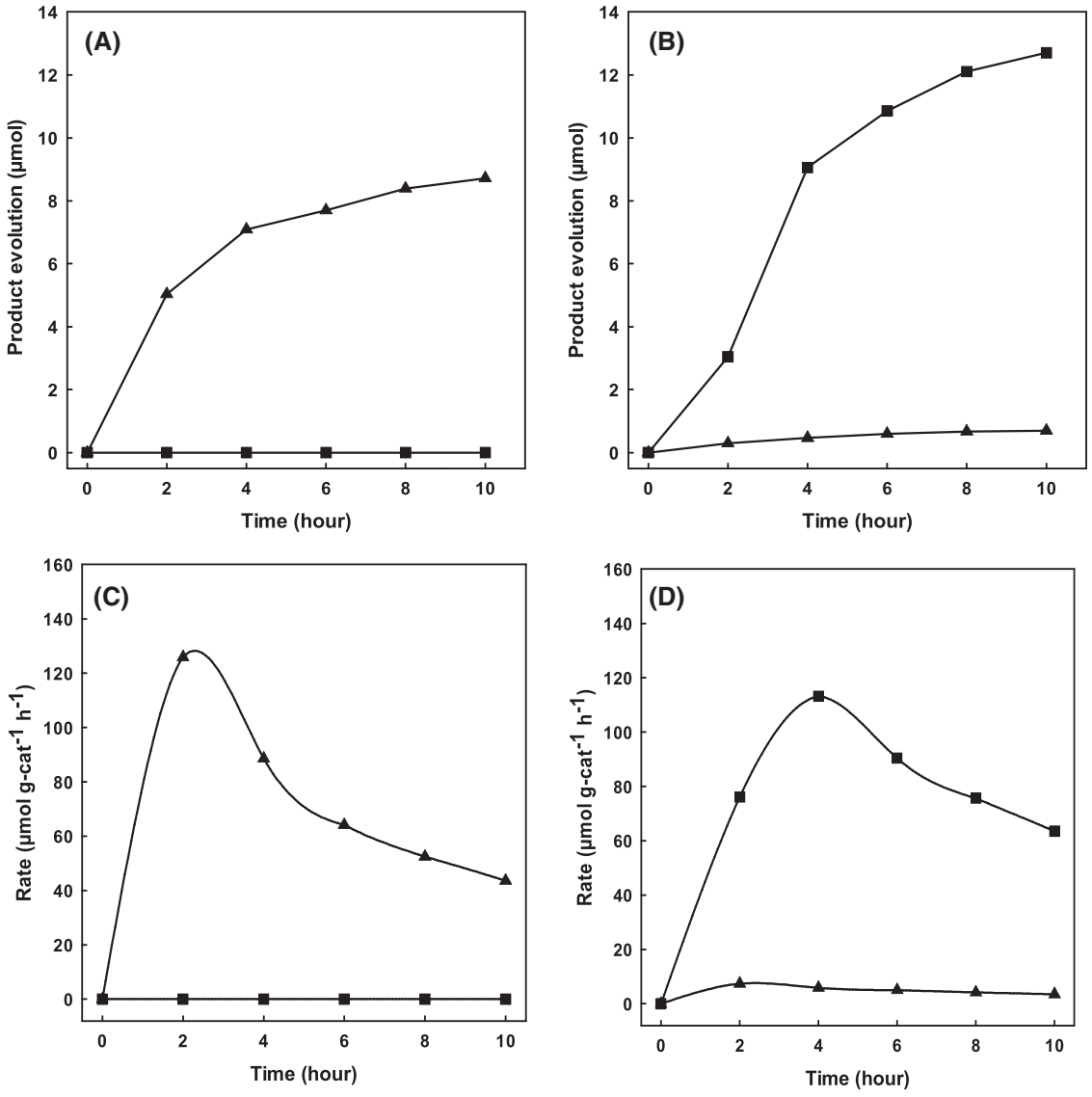

Figure 9. Product evolution and reaction rate A, C) for R-Pt/CNP; B, D) for R-Pt/Cu-CNP (▲ CH_3OH, ■ C_2H_5OH).

highest rate after 2 h, while the formation of ethanol takes a longer time to reach the maximum rate (about 4 h). To investigate the photocatalytic repeatability of the R-Pt/Cu-CNP catalyst, the photocatalytic reduction of CO_2 was performed for three cycles (see **Figure 10**). After each cycle, the photocatalyst was taken out from the reactor and dried at 75 °C in the oven for 1 h. Meanwhile, the system was purged by N_2 to remove all the reactants and products. Subsequently, the mixture of CO_2 and water vapor was reintroduced into the reactor. The results revealed that similar activities for the formation of ethanol and methanol were observed in the second and third cycles.

In the present work, the contents of Cu and Pt were optimized to obtain the best photocatalyst. Our test results showed that the reduced catalyst loaded with ≈2% of Pt and 1% of Cu showed the best photoactivity for the reduction of CO_2. An increase in the Pt and Cu content led to the formation of bigger particles which would cover the surface of R-CNP and prevent the light absorption, resulting in a decrease of photoactivity. On the other hand, the further increase in Cu content might reduce the efficiency of H_2 reduction and hinder the electron transfer between R-CNP and Pt particles, even though it increases the CO_2 adsorption.

3. Mechanism of CO_2 Photoreduction

Based on the obtained results, a possible mechanism is proposed for photocatalytic reduction of CO_2 over R-Pt/CNP and R-Pt/Cu-CNP. Under sunlight, the holes and electrons are generated in VB band and CB band of CNP, respectively. These charges then migrate to the surface to react with reactants. The CO_2 photoreduction at the surface of R-Pt/CNP and R-PtCu/CNP samples includes two parallel processes: the oxidation of water involving VB holes (Equation (1)) and the reduction of CO_2 involving an equivalent number of CB electrons and protons (Equations (2) and (3)) (vs NHE, pH = 7)

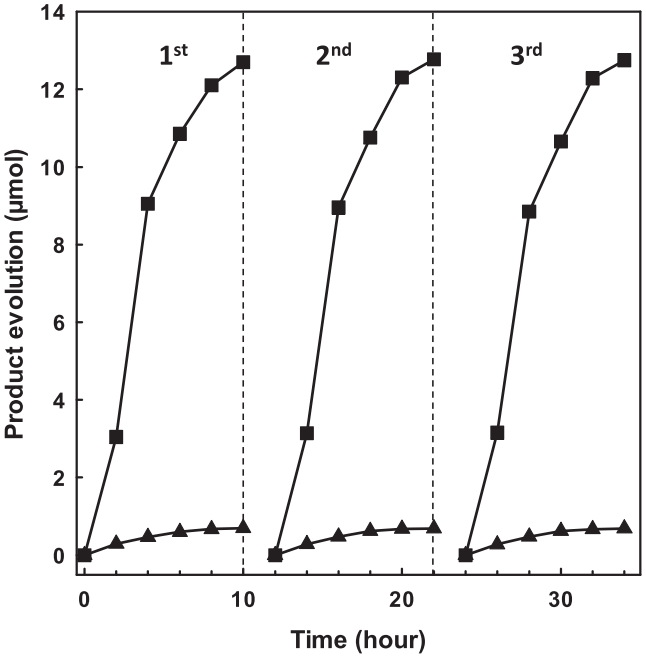

Figure 10. Product evolution of R-Pt/Cu-CNP catalyst for three cycles (▲ CH_3OH, ■ C_2H_5OH).

$$H_2O + 4h^+ \rightarrow O_2 + 4H^+, \quad E^0 = 0.81\ V \tag{1}$$

$$CO_2 + 6H^+ + 6e^- \rightarrow CH_3OH + H_2O, \quad E^0 = -0.38\ V \tag{2}$$

$$2CO_2 + 12H^+ + 12e^- \rightarrow CH_3CH_2OH + 3H_2O, \quad E^0 = -0.33\ V \tag{3}$$

The CO_2 reduction is a multielectron reaction involving some 6 and 12 electrons for methanol and ethanol formation, respectively, with the corresponding value of reduction potential and number of protons. Nevertheless, there is little evidence in the literature for multielectron transfer process in semiconductor photocatalyst.[27] Hence, the photoreduction of CO_2 may proceed through a series of single-electron steps involving the formation of anion radical $CO_2^{\bullet-}$, which is regarded as the most important step in the mechanism of this reduction. However, the addition of an electron to activate CO_2 is a difficult reaction because CO_2 is a chemically quite stable gas with linear geometry and closed-shell electronic configuration.[28] Furthermore, the potential of single electron reduction of CO_2 to anion radical $CO_2^{\bullet-}$ (Equation (4)) is −1.9 V (vs NHE, pH = 7), which is more negative than CB level of all present semiconductors, thus the transfer of an electron to free CO_2 molecule is highly impossible on semiconductor photocatalysts[29]

$$CO_2 + 1e^- \rightarrow CO_2^{\bullet-}, \quad E^0 = -1.9\ V \tag{4}$$

Interestingly, the absorption of CO_2 on the surface of photocatalysts facilitates its single-electron reduction because the interaction between adsorbed CO_2 and surface atoms leads to the formation of charge species $CO_2^{\delta-}$ with some distortion in geometry, which results in a lower barrier for accepting electron.[28,30] Thus, it is significant to observe that the improvement of CO_2 adsorption will enhance its photoconversion into alternative fuels.

Based on the nanostructure of R-Pt/Cu-CNP and the results of CO_2 photoconversion (Table 2), the enhanced photoreduction of CO_2 is ascribed to the unique nanostructure of this photocatalyst, resulting in favorable properties. As illustrated in TEM images (Figures 2 and 4), R-Pt/Cu-CNP having nanosize exhibits very high specific area (up to 210 $m^2\ g^{-1}$), which yields more exposed active sites for the adsorption and reduction of CO_2. Notably, the introduction of Ta^{+4} and/or oxygen vacancies effectively improves the optical properties and activity of R-Pt/Cu-CNP for CO_2 photoreduction. According to its UV–vis spectrum (Figure 6), R-Pt/Cu-CNP shows an apparent enhancement in sunlight absorption likely associated with the presence of the reduced state Ta^{4+} and/or oxygen vacancies. Additionally, the interaction between absorbed CO_2 and oxygen vacancy sites is stronger than with regular sites because the vacancy is healed by the oxygen atom of CO_2 molecule.[31] Thus, the introduction of oxygen vacancies promotes the adsorption and electron transfer to CO_2 in the activation step as well. On the other hand, Pt-rich nanoparticles in the photocatalyst play the role of an active site to achieve a good photoactivity. The difference of Fermi levels between Pt and R-CNP leads to the formation of the Schottky barrier at the interface of Pt and R-CNP, which thus promotes charge separation by allowing the photogenerated electrons in the R-Pt-CNP to be trapped on the Pt nanoparticles.[2a] Moreover, according to TEM images (Figure 4), nanosized Pt-rich particles are in good contact with CNP nanosheets which can shift the Fermi level of R-CNP to a more negative potential, resulting in a high transfer rate of electrons from R-CNP to Pt nanoparticles.[32] The mechanism for the CO_2 reduction over R-Pt-CNP sample is shown in **Figure 11**. In this system, Pt-rich nanoparticles act as the main active sites for CO_2 reduction. After the photon absorption, R-Pt-CNP sample produces electron–hole pairs, the VB holes oxidize H_2O and generate protons and oxygen. These protons continue moving to the reduction side (known as Pt-rich nanoparticles). At the same time, the photogenerated electrons in CB band of R-Pt-CNP easily move to Pt nanoparticles and react to absorb CO_2 in the presence of protons to form methanol.

Copper oxide was added to the reduced nanosheet sample to improve the efficiency of CO_2 photoreduction. As seen in Figure 4, CuO particles may be distributed separately to Pt particles. They have nanosizes and are in close contact to CNP nanosheets. Note that CuO is a p-type semiconductor with a small band gap of 1.7 eV. Hence, coupling CuO and R-CNP may result in the formation of a p–n heterojunction.[33] In detail, the Fermi level in both CuO and R-CNP aligns to reach the equilibrium state. At the equilibrium state, an internal electric field is created at the interface of CuO and R-CNP that can facilitate the transfer of photogenerated holes from the VB of R-CNP to VB of CuO and the reverse transfer of photogenerated electrons from CB of CuO to CB of R-CNP. Additionally, Pt nanoparticles can serve as excellent trapping sites for photogenerated electrons with high transfer rate.[32] Therefore, electron–hole pairs are more effectively separated in R-Pt/Cu-CNP system. Moreover, CuO has been proven to be highly capable of both CO_2 adsorption and reduction due to its highly reactive behavior

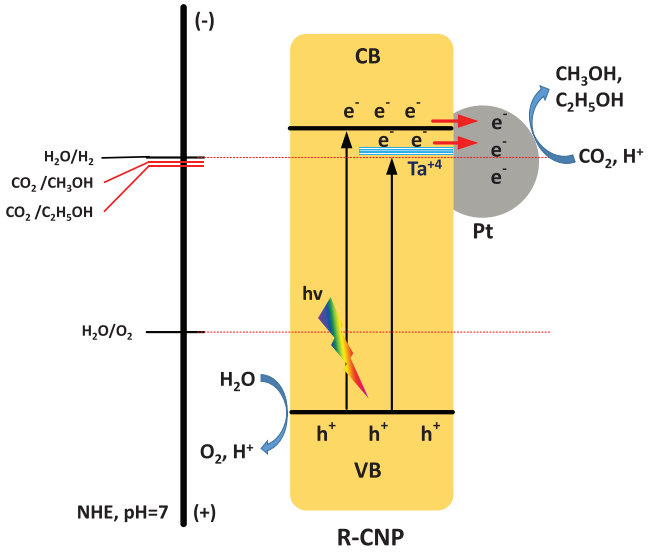

Figure 11. Schematic diagram of CO_2 photoreduction mechanism over R-Pt-CNP system.

toward CO_2 with low adsorption energy.[34] The formation of Pt–Cu alloy nanoparticles is also observed (Figure 5). The synergetic effect of Cu alloying with Pt decreases the work function of nanoparticles, promotes the electron transfer and storage to Pt–Cu alloy particles, thus enhancing the photocatalytic activity.[35] Consequently, R-Pt/Cu-CNP system shows a better photoactivity as compared to R-Pt-CNP system.

The mechanism for CO_2 reduction over R-Pt/Cu-CNP system is illustrated in **Figure 12**. Both Pt and alloy Pt–Cu nanoparticles can act as electron trapping sites and the main active sites for CO_2 reduction, while CuO nanoparticles are the main active sites for water oxidation. Under sunlight, R-Pt/Cu-CNP systems generate electron–hole pairs. The photogenerated holes migrate from VB of R-CNP to VB of CuO react with the adsorbed water molecules and produce protons. Meanwhile, photogenerated electrons trapped in Pt or alloy Pt–Cu nanoparticles undergo a series of electron-transfer processes with the adsorbed CO_2 to form the final product.

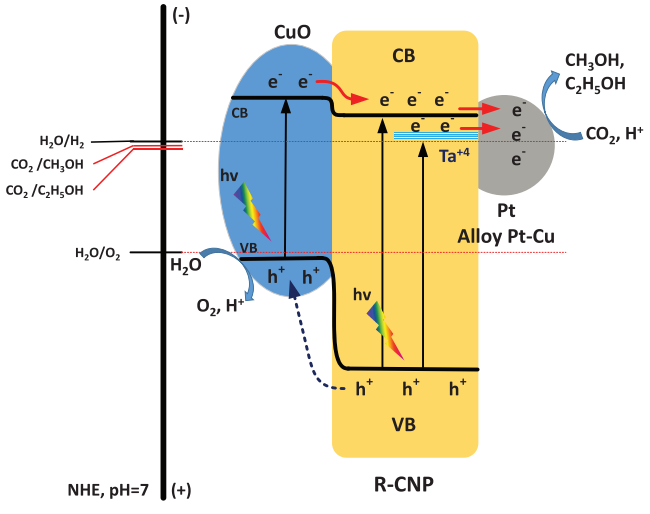

Figure 12. Schematic diagram of CO_2 photoreduction mechanism over R-Pt-CNP.

It should be noted that the composition of the final product is quite different between R-Pt-CNP and R-Pt/Cu-CNP. Methanol is observed as the unique product in the CO_2 photoreduction over R-Pt-CNP system, whereas, over R-Pt/Cu-CNP system, the CO_2 photoreduction produces primarily ethanol and only a small amount of methanol is observed. In the R-Pt-CNP, absorbed CO_2 receives one electron to form $CO_2^{\bullet-}$ anion radical which is converted to C1 intermediates with proton–electron transfer and then reduced to methanol. For the R-Pt/Cu-CNP system, the formation of a high percentage of ethanol, as a C2 compound, suggests a C—C coupling of $CO_2^{\bullet-}$ anion radical C1 intermediates with another nearby intermediate during the reaction. Concerning a possible mechanism for R-Pt/Cu-CNP system, the introduction of both oxygen vacancies and CuO nanoparticles stabilizes C1 intermediates and thus promotes the C—C coupling of nearby intermediates to form C2 intermediates. These C2 intermediates would continue to be reduced within the electron–proton transfer, resulting in the formation of ethanol as the major product. Notably, although the methanol formation rate of reduced nanosheets loaded with Pt (R-Pt-CNP) is higher than the ethanol formation rate of reduced nanosheets loaded with Pt and Cu (R-Pt/Cu-CNP), CO_2 photoconversion is smaller. This is due to the stoichiometry of CO_2 photoreduction as seen in Equations (2) and (3). The formation of one methanol molecule needs only one CO_2 molecule, while two CO_2 molecules are required for one ethanol molecule product.

4. Conclusion

In this study, reduced $HCa_2Ta_3O_{10}$ perovskite nanosheets loaded with Pt and Cu have been developed for photoconversion of CO_2 under solar irradiation. Methods used for synthesis include exfoliation from bulk layered perovskite and H_2 treatment. Physical properties of the resulting nanomaterials were characterized by XRD, SEM, and TEM/HRTEM, BET, UV–vis spectroscopy, and XPS. The obtained nanosheets had a small size and high specific surface area (≈200 m^2 g^{-1}, even after calcination and reduction at 550 °C). The photocatalytic performance of the resulting reduced perovskite nanosheets was evaluated for CO_2 photoreduction under simulated sunlight in the presence of saturated water vapor. The reduced nanosheets exhibited much higher photoactivity than the nonreduced one. This can be ascribed to their unique structure and variety of favorable properties. The hydrogen treatment in the presence of Pt-rich nanoparticles generates a considerable amount of Ta^{+4} and/or oxygen vacancies, which apparently improves the visible light absorption of perovskite nanosheets. Moreover, the introduction of CuO nanoparticles significantly improves the electron–hole separation through the formation of a p–n junction. On the other hand, it enhances the adsorption of CO_2 and stabilizes C1 intermediates as well that is favorable for C—C coupling to form C2 products (e.g., ethanol). Formation rates of ethanol and methanol of 113 and 7.4 μmol g^{-1} h^{-1}, respectively, were observed. By contrast, only methanol was obtained at the rate of 125.9 μmol g^{-1} h^{-1} in the absence of CuO nanoparticles.

In summary, the present research is expected to be useful in the development of efficient photocatalysts and provides meaningful information for further studies of the sunlight-driven conversion of CO_2.

5. Experimental Section

Synthesis of Catalyst: The synthesis of reduced Pt/Cu–$HCa_2Ta_3O_{10}$ nanosheets consists of two stages (Figure S1, Supporting Information).

Synthesis of Catalyst—Synthesis of Bulk Layered Perovskite $CsCa_2Ta_3O_{10}$: Dion–Jacobson type layered perovskite of bulk $CsCa_2Ta_3O_{10}$ was synthesized by solid state reaction using Cs_2CO_3 (99% Sigma), $Ca(CH_3COO)_2.xH_2O$ (99% Sigma), Ta_2O_5 (99.9% Sigma) with an equivalent molar ratio of 1:4:3.[13] Note that an excess amount of Cs_2CO_3 (50 mol%) was added to compensate for the loss of Cs by volatilization. The precursor mixture was thoroughly mixed in ethanol solution (95% in water) and dried overnight at 80 °C before calcination at 1000 °C for 10 h.

Synthesis of Catalyst—Synthesis of Reduced Cu/Pt–$HCa_2Ta_3O_{10}$ Nanosheets (Denoted as R-Pt/Cu-CNP): The obtained bulk layered perovskite was shaken in 3 M HCl solution for one week to exchange Cs ions with protons. The protonated powder (H-$CsCa_2Ta_3O_{10}$) was then washed several times with water before stirring in 0.025 M tetra butyl ammonium hydroxide (TBA-OH) solution to obtain TBA–bulk perovskite. Subsequently, the mixture was placed in an ultrasonic bath for 48 h and then centrifuged at 6500 rpm to remove the excess unexfoliated powder. The solution after centrifugation containing suspended nanosheets was dried thoroughly to obtain nanosheet powder TBA–$HCa_2Ta_3O_{10}$ (denoted as TBA-CNP). TBA was removed by calcination at 550 °C for 4 h to obtain calcined nanosheets (denoted as Cal-CNP). Reduced Cu/Pt–$HCa_2Ta_3O_{10}$ nanosheets (denoted as R-Pt/Cu-CNP) were then prepared by impregnation. Typically, 100 mg of CNP was added to 100 mL aqueous solution containing 4.20 mg of H_2PtCl_6 and 2.10 mg of $CuCl_2$ (corresponding to 2 and 1 wt% of Pt and Cu, respectively). The slurry was maintained at 80 °C under vigorous stirring until all water was vaporized. The remaining solid (containing Pt/Cu loaded $HCa_2Ta_3O_{10}$ nanosheets) was reduced under flowing H_2 (100 mL min^{-1}) at 550 °C for 6 h to obtain the final material. To determine the various oxidation states of Ta, another sample (designated as in situ R-Pt/Cu-CNP) was prepared by H_2 reduction of $HCa_2Ta_3O_{10}$ nanosheets loaded with Pt/Cu at 550 °C for 6 h in the reaction chamber of the XPS spectrometer before performing XPS analysis. To investigate the role of Cu in photoactivity, reduced Pt–$Ca_2Ta_3O_{10}$ nanosheets (R-Pt-CNP) with 2% Pt were also prepared in a similar way and used for comparison with R-Pt/Cu-CNP.

Characterization: SEM and TEM images of the samples were obtained using a JEOL 6360 microscope operated at 15 kV and JOEL JEM 1230 operated at 120 kV, respectively. N_2 adsorption–desorption isotherms of the samples were obtained at –196 °C using a Quantachrome Autosorb-1 MP analyzer. Before the measurements, the samples were outgassed under vacuum for 6 h at 150 °C. XRD patterns of the samples were obtained on a Bruker SMART APEXII X-ray diffractometer equipped with a Cu Kα radiation source (λ = 1.5418 Å). The UV–vis spectra were recorded on a Cary 300 Bio UV–visible spectrophotometer. Finally, XPS measurements were carried out in the ion-pumped chamber (evacuated to 10^{-9} Torr) of a photoelectron spectrometer (Kratos Axis-Ultra) equipped with a focused X-ray source (Al Kα, $h\nu$ = 1486.6 eV).

Photocatalytic Test: The photocatalytic reaction was carried out in an in situ closed circulation system (Figure S2, Supporting Information). The photocatalyst powder was deposited on a circular quartz plate (with a diameter of 3 cm) placed inside the photoreactor which was connected to a six-port gas sampling valve (V = 1 mL) of Agilent gas chromatography system through a circulation pump. Abet model 11002 SunLite Solar Simulator using 150 W Xe arc lamp was used as the light source which provides simulated sunlight of 100 mW cm^{-2}. The reactor system was first purged for 30 min with N_2 (99.5% Praxair) and then a mixture of CO_2 saturated with H_2O vapor, which was generated by passing a high purity CO_2 gas flow (99.99% Praxair) through a water bubbler, was continuously flowed through the reactor for a period of 1 h. All outlet valves were then closed to seal the reactor, and the total pressure was regulated to 1 atm. The reactor was also provided with an external recirculation system (see Figure S2 in the Supporting Information) comprising a recirculation pump, a sampling loop, and a water container which allowed keeping the gaseous reaction medium water saturated. A gaseous sample (1 mL) could then be automatically GC analyzed at given time interval.

The relative CO_2 concentration (C/C_0) evolution was calculated using the following equation

$$C_t/C_0 = \frac{n_{CO_2\,consumed}}{n_{0CO_2}} \times 100 \quad (5)$$

$n_{CO_2\,consumed}$: Molar number of CO_2 consumed for the formation of products, n_{0CO_2}: Initial molar number of CO_2.

Supporting Information

Supporting Information is available from the Wiley Online Library or from the author.

Acknowledgements

This work was supported by the Natural Science and Engineering Research Council of Canada (NSERC) through the Collaborative Research and Development (CRD), Strategic Project (SP), and Discovery Grants. The authors would like to thank EXP Inc. and SiliCycle Inc. for their support.

Conflict of Interest

The authors declare no conflict of interest.

Keywords

CO_2 photoconversion, H_2 reduction, $HCa_2Ta_3O_{10}$ perovskite nanosheets, sunlight-driven photocatalysis

Received: March 24, 2017
Revised: June 8, 2017
Published online:

[1] J. Goldemberg, *Science* **2007**, *315*, 808.
[2] a) S. N. Habisreutinger, L. Schmidt-Mende, J. K. Stolarczyk, *Angew. Chem., Int. Ed.* **2013**, *52*, 7372; b) W. Tu, Y. Zhou, Z. Zou, *Adv. Mater.* **2014**, *26*, 4598.
[3] T. Inoue, A. Fujishima, S. Konishi, K. Honda, *Nature* **1979**, *277*, 637.
[4] a) A. D. Handoko, K. Li, J. Tang, *Curr. Opin. Chem. Eng.* **2013**, *2*, 200; b) K. Li, X. An, K. H. Park, M. Khraisheh, J. Tang, *Catal. Today* **2014**, *224*, 3.
[5] a) W. Wang, M. O. Tade, Z. Shao, *Chem. Soc. Rev.* **2015**, *44*, 5371; b) M. Ardit, G. Cruciani, M. Dondi, C. Zanelli, in *Perovskites and Related Mixed Oxides*, Wiley-VCH, Weinheim, Germany **2016**, pp. 259–288.
[6] a) E. C. Carroll, O. C. Compton, D. Madsen, F. E. Osterloh, D. S. Larsen, *J. Phys. Chem. C* **2008**, *112*, 2394; b) Y. Ebina, T. Sasaki, M. Harada, M. Watanabe, *Chem. Mater.* **2002**, *14*, 4390;

c) A. Kudo, H. Kato, S. Nakagawa, *J. Phys. Chem. B* **2000**, *104*, 571.
[7] M. Hojamberdiev, M. F. Bekheet, E. Zahedi, H. Wagata, Y. Kamei, K. Yubuta, A. Gurlo, N. Matsushita, K. Domen, K. Teshima, *Cryst. Growth Des.* **2016**, *16*, 2302.
[8] a) C.-T. Dinh, T.-D. Nguyen, F. Kleitz, T.-O. Do, *ACS Nano* **2009**, *3*, 3737; b) C.-T. Dinh, T.-D. Nguyen, F. Kleitz, T.-O. Do, *Chem. Commun.* **2011**, *47*, 7797; c) C.-T. Dinh, T.-D. Nguyen, F. Kleitz, T.-O. Do, *Can. J. Chem. Eng.* **2012**, *90*, 8; d) C.-T. Dinh, M.-H. Pham, Y. Seo, F. Kleitz, T.-O. Do, *Nanoscale* **2014**, *6*, 4819; e) C.-T. Dinh, Y. Seo, T.-D. Nguyen, F. Kleitz, T.-O. Do, *Angew. Chem., Int. Ed.* **2012**, *51*, 6608.
[9] C. A. Gueymard, *Sol. Energy* **2004**, *76*, 423.
[10] X. Li, J. Yu, J. Low, Y. Fang, J. Xiao, X. Chen, *J. Mater. Chem. A* **2015**, *3*, 2485.
[11] X. Chen, L. Liu, F. Huang, *Chem. Soc. Rev.* **2015**, *44*, 1861.
[12] X. Chen, L. Liu, P. Y. Yu, S. S. Mao, *Science* **2011**, *331*, 746.
[13] S. Ida, Y. Okamoto, M. Matsuka, H. Hagiwara, T. Ishihara, *J. Am. Chem. Soc.* **2012**, *134*, 15773.
[14] K. Toda, T. Teranishi, Z.-G. Ye, M. Sato, Y. Hinatsu, *Mater. Res. Bull.* **1999**, *34*, 971.
[15] K. Maeda, M. Eguchi, *Catal. Sci. Technol.* **2016**, *6*, 1064.
[16] C.-C. Nguyen, N.-N. Vu, T.-O. Do, *J. Mater. Chem. A* **2016**, *4*, 4413.
[17] M. Hellwig, A. Milanov, D. Barreca, J.-L. Deborde, R. Thomas, M. Winter, U. Kunze, R. A. Fischer, A. Devi, *Chem. Mater.* **2007**, *19*, 6077.
[18] J. G. S. Moo, Z. Awaludin, T. Okajima, T. Ohsaka, *J. Solid State Electrochem.* **2013**, *17*, 3115.
[19] Z. Wang, C. Yang, T. Lin, H. Yin, P. Chen, D. Wan, F. Xu, F. Huang, J. Lin, X. Xie, M. Jiang, *Energy Environ. Sci.* **2013**, *6*, 3007.
[20] J. Hou, S. Cao, Y. Wu, F. Liang, L. Ye, Z. Lin, L. Sun, *Nano Energy* **2016**, *30*, 59.
[21] X. Pan, M.-Q. Yang, X. Fu, N. Zhang, Y.-J. Xu, *Nanoscale* **2013**, *5*, 3601.
[22] G. Zhu, T. Lin, H. Cui, W. Zhao, H. Zhang, F. Huang, *ACS Appl. Mater. Interfaces* **2016**, *8*, 122.
[23] a) T. Fujino, M. Katayama, K. Inudzuka, T. Okuno, K. Oura, T. Hirao, *Appl. Phys. Lett.* **2001**, *79*, 2716; b) C. Sun, Y. Jia, X.-H. Yang, H.-G. Yang, X. Yao, G. Q. Lu, A. Selloni, S. C. Smith, *J. Phys. Chem. C* **2011**, *115*, 25590.
[24] C.-K. Wu, M. Yin, S. O'Brien, J. T. Koberstein, *Chem. Mater.* **2006**, *18*, 6054.
[25] D. C. B. Alves, R. Silva, D. Voiry, T. Asefa, M. Chhowalla, *Mater. Renewable Sustainable Energy* **2015**, *4*, 2.
[26] a) N. S. McIntyre, M. G. Cook, *Anal. Chem.* **1975**, *47*, 2208; b) S. Ntais, R. J. Isaifan, E. A. Baranova, *Mater. Chem. Phys.* **2014**, *148*, 673.
[27] P. V. Kamat, *J. Phys. Chem. Lett.* **2012**, *3*, 663.
[28] H. J. Freund, M. W. Roberts, *Surf. Sci. Rep.* **1996**, *25*, 225.
[29] W. H. Koppenol, J. D. Rush, *J. Phys. Chem.* **1987**, *91*, 4429.
[30] V. P. Indrakanti, J. D. Kubicki, H. H. Schobert, *Energy Environ. Sci.* **2009**, *2*, 745.
[31] a) J. Lee, D. C. Sorescu, X. Deng, *J. Am. Chem. Soc.* **2011**, *133*, 10066; b) X. Chang, T. Wang, J. Gong, *Energy Environ. Sci.* **2016**, *9*, 2177.
[32] W.-N. Wang, W.-J. An, B. Ramalingam, S. Mukherjee, D. M. Niedzwiedzki, S. Gangopadhyay, P. Biswas, *J. Am. Chem. Soc.* **2012**, *134*, 11276.
[33] a) L. Zhang, Q. Luo, X. Chen, M. S. Tse, O. K. Tan, K. H. H. Li, Y. Y. Tay, C. K. Lim, X. Guo, K. C. Leong, *RSC Adv.* **2016**, *6*, 65038; b) D. Malwal, P. Gopinath, *Catal. Sci. Technol.* **2016**, *6*, 4458; c) L. Li, P. A. Salvador, G. S. Rohrer, *Nanoscale* **2014**, *6*, 24; d) A. E. Kandjani, Y. M. Sabri, S. R. Periasamy, N. Zohora, M. H. Amin, A. Nafady, S. K. Bhargava, *Langmuir* **2015**, *31*, 10922.
[34] J. L. V. Moreno, R. L. Arevalo, M. C. S. Escaño, A. A. B. Padama, H. Kasai, *J. Phys. Soc. Jpn.* **2014**, *84*, 015003.
[35] a) L. Qin, G. Si, X. Li, S.-Z. Kang, *RSC Adv.* **2015**, *5*, 102593; b) Y. Shiraishi, H. Sakamoto, Y. Sugano, S. Ichikawa, T. Hirai, *ACS Nano* **2013**, *7*, 9287; c) J. Hou, H. Cheng, O. Takeda, H. Zhu, *Angew. Chem.* **2015**, *127*, 8600.

